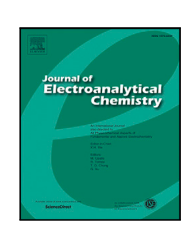
ELSEVIER

Contents lists available at ScienceDirect

Journal of Electroanalytical Chemistry

journal homepage: www.elsevier.com/locate/jeac





Analytical and numerical models for impedance of a button SOFC anode

Marisa Knappe, Andrei Kulikovsky*

Forschungszentrum Jülich GmbH, Theory and Computation of Energy Materials (IET-3), Institute of Energy and Climate Research, D-52425 Jülich, Germany

ARTICLE INFO

Keywords: SOFC Anode Impedance Modeling

ABSTRACT

We report a physics-based model for the anode impedance of a button-type anode-supported SOFC. The model includes ion and electron charge conservation equations and a Fick's diffusion transport equation for hydrogen in the anode support layer. In the limit of small overpotentials, an analytical solution for the anode impedance is derived. For typical SOFC anode parameters, this solution is valid from open–circuit voltage (OCV) up to the cell current density of about 5 mA cm $^{-2}$. Fast least-squares fitting of the model impedance to an experimental spectrum measured at OCV is demonstrated and the resulting fitting parameters are compared with literature data. A high-current numerical version of the model is also suitable for fast fitting of experimental impedance spectra.

1. Introduction

Solid oxide fuel cells (SOFCs) have a number of advantages over low-temperature PEM fuel cells. Perhaps, most important is the ability of SOFCs to operate with methane on the fuel side. Unlike hydrogen, methane is readily available in $\gtrsim 10^8$ households all over the world making development of a residential SOFC unit a highly attractive goal.

Electrochemical impedance spectroscopy (EIS) is one of the most powerful non-destructive tools for fuel cell characterization and testing [1]. Applying a small-amplitude harmonic perturbation to the current and measuring the response of cell potential gives in operando impedance spectrum, which contains virtually all information on the cell transport and kinetic coefficients. However, quite sophisticated physics-based modeling is required to extract these coefficients from the spectra. Here, we do not review the works employing equivalent circuit models (ECM) for spectra analysis (see a review [2]). Models of that type may be not reliable, as discussed by Macdonald in his seminal paper [3]. It should be mentioned that equivalent circuits may work well for description of electrochemical reactions on planar single-crystal electrodes [4]. Here, we discuss the impedance of a finitethickness electrode and transport layer, which are typical for real electrochemical devices such as SOFC. In these systems, simple EC constructed out of resistances, constant phase elements, and Warburg impedances are not reliable.

Early low-current models for impedance of porous electrode employing linear relation for the reaction rate have been developed by Bisquert [5] and by Devan, Subramanian, and White [6]. The authors [6] used concentrated solution theory to describe ionic transport in the liquid electrolyte filling the electrode pores; analytical results they derived are, therefore, rather cumbersome.

Sonn, Leonide, and Ivers-Tiffée [7] used a transmission line to model impedance of SOFC anode. However, to describe depressed semicircles in experimental Nyquist spectra, the constant phase element was used. Similar approach has been taken in the review of Nielsen and Hjelm [8] to discuss the experimental spectra available in literature.

Shi et al. [9] developed a 1d transient macro-homogeneous model for SOFC performance. The cell impedance was calculated by applying AC harmonic perturbation to the cell current, solving the system of partial differential equations (PDE)s in the time domain and performing Fast Fourier Transforms (FFT) of the applied and calculated perturbations. Calculations of this type are quite time-consuming, as every frequency point of the spectrum has to be solved separately. Later, Shi et al. [10] extended their model to two spatial dimensions.

Numerical impedance model with emphasis on methane reforming in the anode chamber has been developed by Zhu and Kee [11]. In their model, the gaseous transport in the electrodes has been calculated using the dusty-gas model, while the charge-transfer reactions have been taken into account using parallel RC-circuit elements with the charge-transfer resistivity calculated from the Butler–Volmer equation. Similar combined approach has been taken by Kromp et al. [12] to study the gas transport effects on SOFC impedance. Hofmann and Panopoulos [13] developed a detailed numerical model for SOFC transient performance based on a commercial CFD solver. The cell impedance was calculated from the Fourier-transformed time-domain solutions.

Bessler [14] suggested applying a small-amplitude potential step to the cell potential, rather than a harmonic perturbation. The advantage of this idea is that the whole impedance spectrum results from a single

E-mail addresses: M.Knappe@fz-juelich.de (M. Knappe), A.Kulikovsky@fz-juelich.de (A. Kulikovsky).

^{*} Corresponding author.

model run, as the step-like function contains all required frequencies in its Fourier-spectrum.

Bessler and Gewies [15] developed a 1d+1d model for hydrogen transport in the anode gas chamber and calculated the anode impedance. The membrane electrode assembly (MEA) has not been resolved in their model; the hydrogen oxidation reaction (HOR) was assumed to take place at the channel wall. The effect of convective and diffusive hydrogen transport in the channel on impedance spectra under linear and non-linear Butler-Volmer kinetics of HOR has been demonstrated. A more accurate 3d model for SOFC anode impedance of that type, with no spatial resolution of MEA has been developed by Haeffelin et al. [16]. Fu et al. [17] reported analysis of multicomponent diffusion in the porous anodes and compared the experimental anode spectra measured at OCV with the model calculations. Recently, Donazzi et al. [18] reported a 1d+1d impedance model of SOFC with the straight channels on either side. In their work, the conservation equations have been linearized and Fourier-transformed and the resulting linear 1d+1d ordinary differential equations (ODEs) for the small perturbation amplitudes have been solved numerically. This approach leads to much faster numerical code. Local impedance spectra at several distances along the channel have been calculated and discussed.

Overall, there is a lack of simple physics-based models for SOFC anode impedance, which would take into account both ionic and electron transport in the electrode and would be valid up to high cell current densities. The model should be fast enough to be used in least-squares algorithms for fitting experimental spectra. To the best of our knowledge, no analytical models for the SOFC anode impedance have been developed so far. The present work aims at filling this gap. The equivalent circuit models are fast for experimental spectra fitting; however, they could lead to misleading results. On the other hand, being quite accurate, the detailed CFD models are time-consuming for using in least-squares fitting algorithms. The impedance model below employs 1d physics-based charge and mass conservation equations. The derived low-current analytical formulas for the anode impedance work well from the open-circuit cell potential up to the cell currents on the order of 5 mA cm⁻². The numerical impedance model is valid up to high cell currents. Fast fitting algorithms can be constructed using either the analytical formulas, or the numerical high-current model.

2. Model

The model below employs the following basic assumptions

- · The cell is isothermal.
- The pressure gradient is small and it does not affect the species transport in porous anode.
- The hydrogen oxidation reaction (HOR) obeys to the Butler-Volmer law. Here, we do not consider detailed reaction mechanisms of HOR.

2.1. Butler-Volmer equation for the hydrogen oxidation reaction

The anodic reaction is

$$H_2 + O^{2-} \leftrightarrow H_2O + 2e^-$$
 (1)

The low-current model below is valid for small current densities, down to open-circuit conditions and hence both the direct and reverse branches of the Butler-Volmer equation have to be taken into account:

$$R_{HOR} = i_* \left(\left(\frac{c_{hy}}{c_{hy,ref}} \right)^{\gamma_{hy}} \exp\left(-\frac{\eta}{b_{hy}} \right) - \left(\frac{c_w}{c_{w,ref}} \right)^{\gamma_w} \exp\left(\frac{\eta}{b_w} \right) \right)$$
 (2)

where

$$\eta = \phi - \Phi \tag{3}$$

is the (negative) HOR overpotential, ϕ and Φ are the electron and ionic phase potentials, respectively, $i_*(T, \lambda_{TPB}^{eff})$ is the exchange current

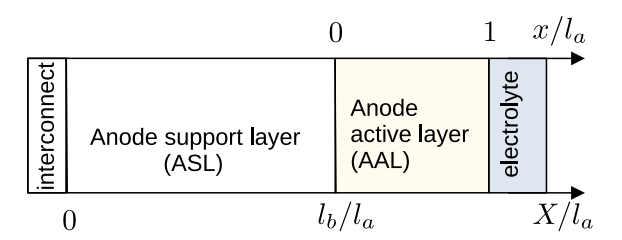


Fig. 1. Schematic of the SOFC anode and the system of coordinates. The *x*-axis is used in the AAL impedance problem. The *X*-axis is employed in the problem with hydrogen transport in the ASL. Note that Figure is strongly not to scale: the ASL thickness is typically two orders of magnitude larger than the AAL thickness.

density, where λ_{TPB}^{eff} is the density of electrochemical active area at the triple phase boundaries, c_{hy} , $c_{hy,ref}$ are the available and reference hydrogen concentrations, γ_{hy} is the HOR reaction order, c_w , $c_{w,ref}$ are the available and reference water vapor concentrations, γ_w is the reaction order of the backward hydrogen evolution reaction (HER) (1), and b_{hy} , b_w are the forward and backward reaction Tafel slopes. The equilibrium potential of HOR is close to zero and hence it can be omitted in the definition of overpotential, Eq. (3).

Unless stated otherwise, below we will assume that in the limit of small cell current, the hydrogen and water concentrations are at their reference values. With this, Eq. (2) simplifies to

$$R_{HOR} \simeq i_* \left(\exp\left(-\frac{\eta}{b_{hv}}\right) - \exp\left(\frac{\eta}{b_{uv}}\right) \right)$$
 (4)

The effect of hydrogen concentration on the anode impedance will be considered in Section 2.5.

2.2. Basic charge conservation equations

In this section, we focus on the anode active layer (AAL) problem. Here, hydrogen transport through the anode support layer (ASL) is ignored; it will be incorporated in Section 2.5. The anode schematic and the system of coordinates are depicted in Fig. 1.

Ionic and electron current conservation equations for the AAL are

$$-C_{dl}\frac{\partial \eta}{\partial t} + \frac{\partial j_i}{\partial x} = -R_{HOR} \tag{5}$$

$$C_{dl}\frac{\partial \eta}{\partial t} + \frac{\partial j_e}{\partial x} = R_{HOR} \tag{6}$$

where C_{dl} is the effective double layer (DL) volumetric capacitance (F cm⁻³), j_i , j_e are the ionic and electron current density (flux), respectively. With the x-axis in Fig. 1 both j_i and j_e are negative.

The Ohm's law for the ionic and electron currents is

$$j_i = -\sigma_i \frac{\partial \Phi}{\partial x}, \quad j_e = -\sigma_e \frac{\partial \Phi}{\partial x}$$
 (7)

where σ_i , σ_e are the AAL ionic and electron conductivities, respectively. It is convenient to introduce dimensionless variables

$$\tilde{x} = \frac{x}{l_a}, \quad \tilde{t} = \frac{ti_*}{C_{dl}b_{hy}}, \quad \tilde{j} = \frac{jl_a}{\sigma_i b_{hy}}, \quad \tilde{\eta} = \frac{\eta}{b_{hy}},$$

$$\tilde{\Phi} = \frac{\Phi}{b_{hy}}, \quad \tilde{\Phi} = \frac{\phi}{b_{hy}}, \quad \tilde{Z} = \frac{Z\sigma_i}{l_a}, \quad \tilde{\omega} = \frac{\omega C_{dl}b_{hy}}{i_*}$$
(8)

where l_a is the AAL thickness, Z is the impedance, and ω is the angular frequency of applied AC perturbation. With the variables (8), Eqs. (4)–(7) transform to

$$\tilde{R} = \exp(-\tilde{\eta}) - \exp(\beta \tilde{\eta}) \tag{9}$$

$$-\frac{\partial \tilde{\eta}}{\partial \tilde{t}} + \varepsilon^2 \frac{\partial \tilde{J}_i}{\partial \tilde{x}} = -\tilde{R} \tag{10}$$

$$\frac{\partial \tilde{\eta}}{\partial \tilde{t}} + \varepsilon^2 \frac{\partial \tilde{j}_e}{\partial \tilde{x}} = \tilde{R} \tag{11}$$

$$\tilde{j}_i = -\frac{\partial \tilde{\Phi}}{\partial \tilde{x}}, \quad \tilde{j}_e = -k_\sigma \frac{\partial \tilde{\phi}}{\partial \tilde{x}},$$
 (12)

where

$$k_{\sigma} \equiv \frac{\sigma_e}{\sigma_i}, \quad \epsilon \equiv \sqrt{\frac{\sigma_i b}{i_* l_a^2}}, \quad \beta \equiv \frac{b_{hy}}{b_w}.$$
 (13)

Substituting Eqs. (12) into Eqs. (10), (11), we get a system of equations for the potentials

$$\frac{\partial \tilde{\eta}}{\partial \tilde{t}} + \epsilon^2 \frac{\partial^2 \tilde{\Phi}}{\partial \tilde{x}^2} = \exp(-\tilde{\eta}) - \exp(\beta \tilde{\eta})$$
(14)

$$\frac{\partial \tilde{\eta}}{\partial \tilde{t}} - k_{\sigma} \varepsilon^{2} \frac{\partial^{2} \tilde{\phi}}{\partial \tilde{x}^{2}} = \exp(-\tilde{\eta}) - \exp(\beta \tilde{\eta})$$
(15)

Subtracting Eq. (15) from Eq. (14) and integrating the resulting equation once, we come to the current balance equation $\tilde{j}_e + \tilde{j}_i = \tilde{j}_0$, where \tilde{j}_0 is the total cell current density.

2.3. Equations for the perturbation amplitudes

Application of a small-amplitude harmonic AC perturbation to the cell potential or current leads to harmonic response of the potentials Φ and ϕ . Mathematically this response can be described as

$$\tilde{\boldsymbol{\Phi}}(\tilde{\mathbf{x}}, \tilde{t}) = \tilde{\boldsymbol{\Phi}}^{0}(\tilde{\mathbf{x}}) + \tilde{\boldsymbol{\Phi}}^{1}(\tilde{\mathbf{x}}, \tilde{\boldsymbol{\omega}}) \exp(i\tilde{\boldsymbol{\omega}}\tilde{t}), \quad |\tilde{\boldsymbol{\Phi}}^{1}| \ll \tilde{\boldsymbol{\Phi}}^{0}$$

$$\tilde{\boldsymbol{\phi}}(\tilde{\mathbf{x}}, \tilde{t}) = \tilde{\boldsymbol{\phi}}^{0}(\tilde{\mathbf{x}}) + \tilde{\boldsymbol{\phi}}^{1}(\tilde{\mathbf{x}}, \tilde{\boldsymbol{\omega}}) \exp(i\tilde{\boldsymbol{\omega}}\tilde{t}), \quad |\tilde{\boldsymbol{\phi}}^{1}| \ll \tilde{\boldsymbol{\phi}}^{0}$$
(16)

where the superscripts 0 and 1 mark the static values and the small perturbation amplitudes, respectively. A standard procedure [19] of linearization and Fourier- transformation of Eqs. (14), (15) using Eqs. (16) yields a system of linear equations for the small perturbation amplitudes $\tilde{\Phi}^1$, $\tilde{\Phi}^1$ in the $\tilde{\omega}$ -space

$$\varepsilon^2 \frac{\partial^2 \tilde{\Phi}^1}{\partial \tilde{x}^2} = -\tilde{Q}^0 \tilde{\eta}^1 - i\tilde{\omega}\tilde{\eta}^1, \quad \tilde{\Phi}^1(1) = 0, \quad \frac{\partial \tilde{\Phi}^1}{\partial \tilde{x}} \bigg|_{\tilde{x}=0} = 0 \tag{17}$$

$$k_{\sigma} \varepsilon^{2} \frac{\partial^{2} \tilde{\phi}^{1}}{\partial \tilde{x}^{2}} = \tilde{Q}^{0} \tilde{\eta}^{1} + i\tilde{\omega}\tilde{\eta}^{1}, \quad \tilde{\phi}^{1}(0) = \tilde{\phi}_{0}^{1}, \quad \frac{\partial \tilde{\phi}^{1}}{\partial \tilde{x}} \bigg|_{z=1} = 0$$
 (18)

where ϕ_0^1 is the applied perturbation amplitude of the anode (electron phase) potential,

$$\tilde{\eta}^1 = \tilde{\phi}^1 - \tilde{\Phi}^1,\tag{19}$$

is the overpotential perturbation amplitude, and

$$\tilde{Q}^0 = \exp\left(-\tilde{\eta}^0\right) + \beta \exp\left(\beta \tilde{\eta}^0\right). \tag{20}$$

is the static variable. At large currents, \tilde{Q}^0 is a strong function of coordinate \tilde{x} (see below). However, for small cell currents, \tilde{Q}^0 can be approximated by a constant value. It is worth noting that with the constant \tilde{Q}^0 , the system (17), (18) formally is identical to the system of equations for the ionomer and carbon phase potential perturbations in the cathode catalyst layer of a PEM fuel cell [19].

By definition, the anode impedance \tilde{Z} is given by

$$\tilde{Z} = \frac{\tilde{\phi}_0^1}{\tilde{j}_{e,0}^1} = \frac{\tilde{\phi}_0^1}{-k_\sigma \partial \tilde{\phi}^1 / \partial \tilde{x}|_{\tilde{x}=0}}.$$
 (21)

2.4. Static equations: Large cell current

At large cell currents, the static shapes $\tilde{\Phi}^0(\tilde{x})$, $\tilde{\Phi}^0(\tilde{x})$ may strongly vary along \tilde{x} . Chalking out the time derivatives in Eqs. (14), (15), we come to equations for $\tilde{\Phi}^0$ and $\tilde{\phi}^0$:

$$\varepsilon^2 \frac{\partial^2 \tilde{\Phi}^0}{\partial \tilde{\mathbf{x}}^2} = \tilde{R}^0, \quad \tilde{\Phi}^0(1) = 0, \quad \frac{\partial \tilde{\Phi}^0}{\partial \tilde{\mathbf{x}}} \Big|_{\tilde{\mathbf{x}} = 1} = -\tilde{f}_0,$$
 (22)

$$k_{\sigma} \varepsilon^{2} \frac{\partial^{2} \tilde{\phi}^{0}}{\partial \tilde{x}^{2}} = -\tilde{R}^{0}, \quad k_{\sigma} \left. \frac{\partial \tilde{\phi}^{0}}{\partial \tilde{x}} \right|_{\tilde{x}=0} = -\tilde{j}_{0}, \quad \left. \frac{\partial \tilde{\phi}^{0}}{\partial \tilde{x}} \right|_{\tilde{x}=1} = 0.$$
 (23)

where

$$\tilde{R}^0 = \exp(-\tilde{\eta}^0) - \exp(\beta \tilde{\eta}^0), \quad \tilde{\eta}^0 = \tilde{\phi}^0 - \tilde{\Phi}^0$$
 (24)

The system of Eqs. (22), (23) determines the static shape of the HOR overpotential $\tilde{\eta}^0$, which appears in Eqs. (17), (18). The strongly nonlinear boundary-value problem (BVP) (22), (23) can only be solved numerically. The static solutions $\tilde{\Phi}^0(\tilde{x})$, $\tilde{\phi}^0(\tilde{x})$ provide coefficients for the linear Eqs. (17), (18), solution of which gives the AAL impedance, Eq. (21).

2.5. Hydrogen transport in the anode support layer

Typically, the AAL is sandwiched between the anode support layer (ASL) and electrolyte, so to reach the AAL, hydrogen must be transported through the ASL (Fig. 1). ASL thickness is large, on the order of 1 mm [20,21] and it typically gives quite a significant contribution to the anode impedance. For simplicity, we will assume that the ASL electron conductivity is large [22].

To take into account the impedance of hydrogen transport in the ASL, we need to include the concentration factor in the AAL charge conservation equations. Assuming that the water concentration is at its reference value, we write Eqs. (14), (15) in the form

$$\frac{\partial \tilde{\eta}}{\partial \tilde{t}} + \epsilon^2 \frac{\partial^2 \tilde{\Phi}}{\partial \tilde{x}^2} = \tilde{c}_* \exp(-\tilde{\eta}) - \exp(\beta \tilde{\eta})$$
 (25)

$$\frac{\partial \tilde{\eta}}{\partial \tilde{t}} - k_{\sigma} \varepsilon^{2} \frac{\partial^{2} \tilde{\phi}}{\partial \tilde{x}^{2}} = \tilde{c}_{*} \exp(-\tilde{\eta}) - \exp(\beta \tilde{\eta})$$
 (26)

where $\tilde{c}_* = c_*/c_{ref}$ is the dimensionless hydrogen concentration at the ASL/AAL interface. Since the AAL thickness is small as compared to the ASL one, we may assume that the hydrogen transport in the AAL is fast, hence the static and perturbed hydrogen concentrations are constant through the AAL depth.

Linearization and Fourier-transformation of Eqs. (25), (26) leads to

$$\varepsilon^2 \frac{\partial^2 \tilde{\varPhi}^1}{\partial \tilde{x}^2} = - \left(\tilde{\mathcal{Q}}_c^0 + \mathrm{i} \tilde{\omega} \right) \tilde{\eta}^1 \ + \tilde{R}_c^0 \tilde{c}_*^1, \label{eq:epsilon_epsilon}$$

$$\tilde{\Phi}^{1}(1) = 0, \quad \frac{\partial \tilde{\Phi}^{1}}{\partial \tilde{x}} \Big|_{\tilde{x}=0} = 0$$
 (27)

$$k_{\sigma} \varepsilon^2 \frac{\partial^2 \tilde{\phi}^1}{\partial \tilde{x}^2} = \left(\tilde{Q}_c^0 + \mathrm{i} \tilde{\omega} \right) \tilde{\eta}^1 - \tilde{R}_c^0 \tilde{c}_*^1,$$

$$\tilde{\phi}^1(0) = \tilde{\phi}_0^1, \quad \frac{\partial \tilde{\phi}^1}{\partial \tilde{x}} \bigg|_{\tilde{x}=1} = 0$$
 (28)

Here \tilde{c}_*^1 is the perturbation of hydrogen concentration at the ASL/AAL interface, and

$$\begin{split} \tilde{R}_c^0 &= \tilde{c}_*^0 \exp(-\tilde{\eta}^0) - \exp(\beta \tilde{\eta}^0) \\ \tilde{Q}_c^0 &= \tilde{c}_*^0 \exp(-\tilde{\eta}^0) + \beta \exp(\beta \tilde{\eta}^0) \end{split} \tag{29}$$

where

$$\tilde{c}_{*}^{0} = \tilde{c}_{hy,a} \left(1 - \frac{j_0}{j_{\text{lim}}} \right), \quad j_{\text{lim}} = \frac{2FD_b c_{hy}}{l_b}$$
 (30)

takes into account static hydrogen transport through the ASL, and $\tilde{c}_{hy,a}$ is the hydrogen concentration in the anode channel. Eqs. (27), (28) formally differ from the problem Eqs. (17), (18) by the term $\tilde{R}_c^0 \tilde{c}_*^1$ on the right side.

The parameter \tilde{c}_*^1 can be determined from the transient Fick's diffusion equation in the ASL. With the dimensionless variables (8) this equation is

$$\mu^2 \frac{\partial \tilde{c}_b}{\partial \tilde{t}} - \epsilon^2 \tilde{D}_b \frac{\partial^2 \tilde{c}_b}{\partial \tilde{X}^2} = 0 \tag{31}$$

where the coordinate \tilde{X} is counted from the interconnect (Fig. 1), μ is the dimensionless parameter

$$\mu = \sqrt{\frac{2Fc_{ref}}{C_{dl}b_{hy}}},\tag{32}$$

 \tilde{c}_b is the hydrogen concentration in the ASL, and \tilde{D}_b is the dimensionless ASL hydrogen diffusivity given by

$$\tilde{D}_b = \frac{2FD_b c_{ref}}{\sigma_i b_{hy}}. (33)$$

Eq. (31) is linear and hence Fourier-transformation of this equation gives

$$\varepsilon^2 \tilde{D}_{hy} \frac{\partial^2 \tilde{c}_b^1}{\partial \tilde{X}^2} = \mathrm{i} \tilde{\omega} \mu^2 \tilde{c}_b^1, \quad \tilde{c}_b^1(0) = 0, \quad \tilde{D}_b \frac{\partial \tilde{c}_b^1}{\partial \tilde{X}} \bigg|_{\tilde{X} = \tilde{I}_e} = \tilde{J}_{e,0}^1 \tag{34}$$

where \tilde{l}_b is the dimensionless ASL thickness

$$\tilde{l}_b = \frac{l_b}{l_a}. (35)$$

The left boundary condition for Eq. (34) means zero perturbation of the hydrogen concentration in the anode channel. This assumption works well provided that the hydrogen stoichiometry is large. The right boundary condition for Eq. (34) is consistent with the assumption of fast hydrogen transport in the AAL and it simply means the stoichiometric requirement for the hydrogen flux perturbation. Here, $\tilde{j}_{e,0}^1$ is the electron current perturbation amplitude at the interconnect; since the ASL electron conductivity is assumed to be high, $\tilde{j}_{e,0}^1$ coincides with the electron current perturbation at the ASL/AAL interface.

3. Results and discussion

3.1. Small cell current density: Analytical impedance

Let the cell current density be small, meaning that the variation of overpotential $\tilde{\eta}^0$ along \tilde{x} is small. Assuming that \tilde{Q}^0 , Eq. (20), is constant, Eqs. (17), (18) form a system of linear second-order ODEs with the constant coefficients. Solution of this system is straightforward and it results in

$$\tilde{Z} = \frac{\left(1 + k_{\sigma}^{2}\right) \coth(p) + k_{\sigma}\left(p + 2/\sinh(p)\right)}{p k_{\sigma}(1 + k_{\sigma})}$$
 (36)

where

$$p \equiv \frac{1}{\varepsilon} \sqrt{\left(1 + 1/k_{\sigma}\right) \left(\tilde{Q}^{0} + i\tilde{\omega}\right)}. \tag{37}$$

Eq. (36) in a different form has been derived in [19] in the context of PEM fuel cells.

Neglecting ionic transport losses, the estimate of static overpotential \tilde{p}^0 for calculation of \tilde{O}^0 can be obtained from Eq. (24):

$$|\tilde{j}_0| = \tilde{R}^0 \tag{38}$$

At small currents, the absolute value of overpotential $\tilde{\eta}^0$ is small and \tilde{R}^0 , Eq. (9), can be expanded in Taylor series at $\tilde{\eta}^0=0$. Keeping two leading terms, from Eq. (38) we get

$$\tilde{\eta}^0 \simeq -\frac{|\tilde{J}_0|}{1+\beta} \tag{39}$$

Eq. (36) is valid provided that the cell current density $|j_0|$ is much less than the least of characteristic current densities of ionic and electron transport in the anode:

$$|j_0| \ll \min\left\{\frac{\sigma_i b_{hy}}{l_a}, \frac{\sigma_e b_{hy}}{l_a}\right\} \tag{40}$$

The anode ionic conductivity is usually much smaller than the electronic one and Eq. (40) reduces to

$$|j_0| \ll \frac{\sigma_i b_{hy}}{l_a} \tag{41}$$

For the parameters in Table 1, we get $|j_0| \ll 20~\text{mA cm}^{-2}$, i.e., Eq. (36) is accurate up to the cell currents $\simeq 5~\text{mA cm}^{-2}$. Note that since the AAL conductivity is a strong function of temperature, Eq. (41) depends on the cell temperature as well.

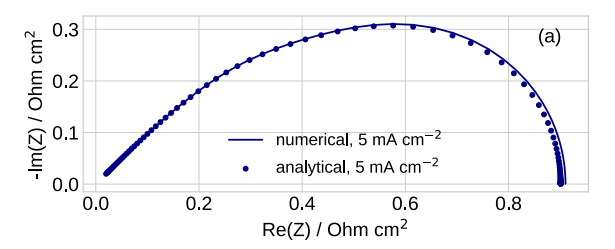
In the limit of high AAL electron conductivity we set $k_\sigma \to \infty$ and Eq. (36) simplifies to [23]

$$\tilde{Z}_{k_{\sigma} \to \infty} = \frac{1}{\sqrt{\left(\tilde{Q}^{0} + i\tilde{\omega}\right)/\epsilon^{2}} \tanh\left(\sqrt{\left(\tilde{Q}^{0} + i\tilde{\omega}\right)/\epsilon^{2}}\right)}$$
(42)

Table 1

The cell parameters used in calculations. AAL and ASL stand for the anode active layer and anode support layer, respectively. The volumetric C_{dl} used in this work is related to the superficial double layer capacitance $C_{dl,s}$ as $C_{dl} = C_{dl,s}/I_a$.

-ai,s ai -ai,s ai	
Cell temperature T, K	1073
Hydrogen pressure p_{hv} , bar	1
Reference H_2 pressure, $p_{hy,ref}$, bar	0.2
Water vapor pressure p_w , bar	0.01
Reference water pressure $p_{w,ref}$, bar	0.01
HOR Tafel slope b, V /exp	0.1
Double layer capacitance C_{dl} , F cm ⁻³	2
Exchange current density i_* , A cm ⁻³	100
AAL ionic conductivity σ_i , S cm ⁻¹	$1 \cdot 10^{-3}$
AAL electron conductivity σ_e , S cm ⁻¹	$4.2 \cdot 10^{4}$
AAL thickness l_a , cm	$15 \cdot 10^{-4}$
ASL thickness l_b , cm	0.15
ASL hydrogen diffusivity D_b , cm ² s ⁻¹	0.1
Parameter $\beta = b_{hy}/b_w = \alpha_w/\alpha_{hy}$ [24]	1/3



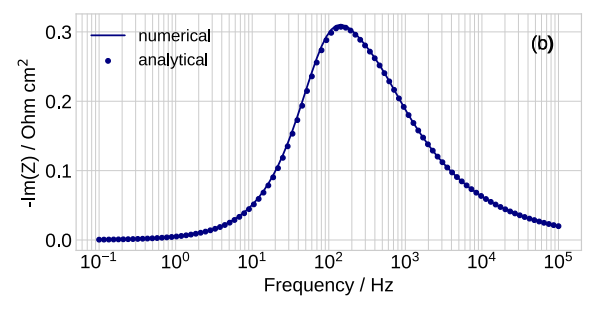


Fig. 2. (a) The numerical (line) and analytical (points) Nyquist spectra of the anode for the cell current density of 5 mA cm $^{-2}$. The other parameters for calculations are listed in Table 1. (b) The Bode plot of imaginary part of impedance in (a).

With the electron conductivity six orders of magnitude higher than the ionic conductivity (Table 1), the spectra of Eqs. (36) and (42) are indistinguishable.

The high-frequency AAL resistance R_{HFR} is obtained from Eq. (36) in the limit of $\tilde{\omega} \to \infty$. Calculation gives

$$\frac{1}{R_{HFR}} = \frac{1}{l_a/\sigma_i} + \frac{1}{l_a/\sigma_e} \tag{43}$$

which is the AAL ionic $R_i=l_a/\sigma_i$ and electronic $R_e=l_a/\sigma_e$ resistivities connected in parallel. Note that for $\sigma_e\to\infty$, we get $R_{HFR}\to0$.

Fig. 2 compares the analytical and numerical spectra of SOFC anode active layer for the parameters listed in Table 1 and the current density of 5 mA cm⁻². The numerical spectrum is calculated taking into account the variation of static parameters along \tilde{x} (see next Section). As can be seen, at 5 mA cm⁻², Eq. (36) is quite accurate. As expected, calculations show that at lower currents the agreement is better.

Fig. 3 shows the shapes of static potentials of the electrolyte and electron phase through the AAL depth derived from the numerical solution of the system (22), (23) (see next Section). Due to the large electron conductivity σ_e , the electron phase potential ϕ^0 is highly uniform through the anode; however, the ionic phase potential ϕ^0 varies with \tilde{x} quite significantly. From Fig. 3 it follows that the absolute value of static overpotential at the electrolyte interface is about three

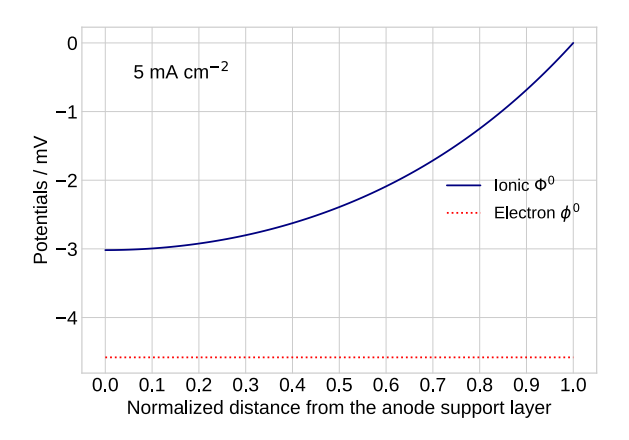


Fig. 3. The shapes of static potentials of the electrolyte phase Φ^0 and electron phase ϕ^0 for the cell current density of 5 mA cm⁻² and the other parameters listed in Table 1. $\tilde{x} = 1$ is at the electrolyte surface.

times higher than at the ASL/AAL interface. Nonetheless, due to $\tilde{\eta}^0$ smallness, the approximation $\tilde{Q}^0 \simeq \text{const}$ works well.

3.2. Large cell current density

Consider now the case of large cell current density, when the variation of overpotential $\tilde{\eta}^0$ along \tilde{x} cannot be neglected. Let the hydrogen and water vapor concentrations be uniform through the AAL depth and equal to their reference values.

The AAL impedance for the cell current density of 1 A cm $^{-2}$ calculated from numerical solution of Eqs. (17), (18), (22), (23) is depicted in Fig. 4. The Nyquist spectrum shape is quite similar to the low-current spectrum in Fig. 2a; however, the peak of imaginary part is strongly shifted to higher frequencies (cf. Figs. 2b and 4b). Note that the cell polarization resistance R_{pol} (the Nyquist spectrum diameter) strongly decreases with the cell current density (cf. Figs. 2a and 4a). From the Tafel law it follows that the contribution of HOR to R_{pol} is given by b_{hy}/j_0 , where b_{hy} is the HOR Tafel slope and j_0 is the cell current density. Inverse proportionality of R_{pol} to the cell current explains the effect.

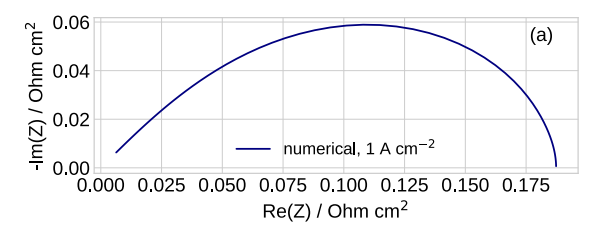
At 1 A cm⁻², the shape of static potentials through the electrode depth (Fig. 5) are qualitatively quite similar to those shapes at low current. However, the absolute value of potentials at high current is much larger (cf. Figs. 3 and 5).

The high-current numerical model works for any cell current density, provided that the basic assumptions hold. For example, the model in its present form does not work if a significant temperature gradient forms in the electrode. This would lead to dependence of ionic conductivity on the distance from electrolyte; however, this effect could be incorporated into the model.

Another assumption that needs to be checked is fast hydrogen transport in the AAL. The gradient of $\rm H_2$ concentration can be neglected if the cell current density is much less than the characteristic transport current density given by

$$j_{hy,tr} = \frac{2FD_{hy}c_{hy}}{l_a} \tag{44}$$

For the estimate we take $D_{hy}=D_b$ and the other parameters from Table 1. This gives $j_{hy,tr}=144~{\rm A~cm^{-2}}$. Thus, the hydrogen concentration is nearly uniform through the AAL depth for all realistic cell current densities.



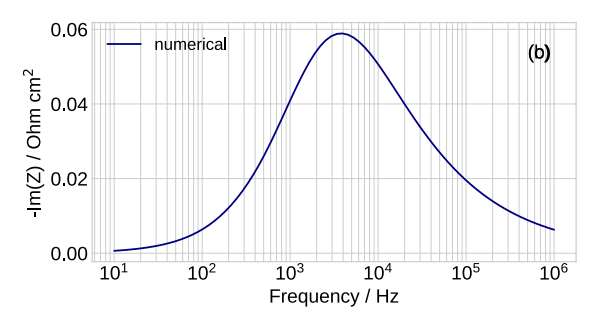


Fig. 4. (a) The numerical Nyquist spectrum of the anode for the cell current density of 1 A cm $^{-2}$. The other parameters for calculations are listed in Table 1. (b) The Bode plot of imaginary part of impedance in (a).

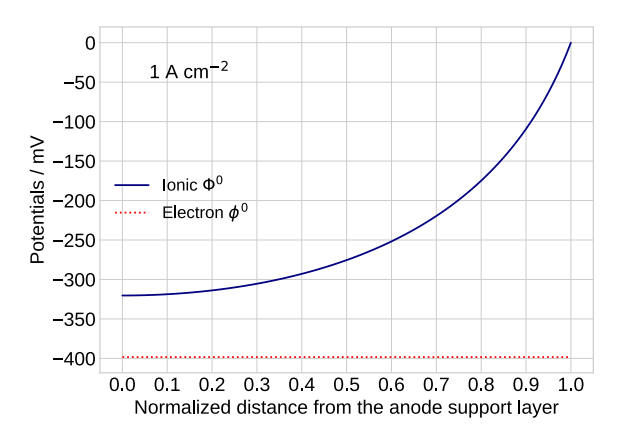


Fig. 5. The shapes of static potential of the electrolyte phase Φ^0 and electron phase ϕ^0 for the cell current density of 1 A cm⁻². The other parameters are listed in Table 1.

3.3. Analytical anode impedance including hydrogen transport in the support layer

Solving Eq. (34) and setting $\bar{X} = \tilde{l}_b$ in the solution we get the perturbation amplitude of hydrogen concentration at the ASL/AAL interface $\tilde{c}_*^1 = \tilde{c}_b^1(\tilde{l}_b)$:

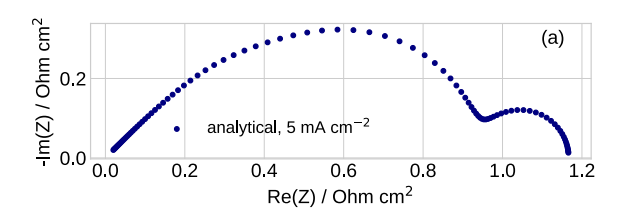
$$\tilde{c}_*^1 = \tilde{Z}_W \tilde{j}_{e\,0}^1 \tag{45}$$

where

$$\tilde{Z}_{W} = \frac{\tanh\left(\mu \tilde{l}_{b} \sqrt{i\tilde{\omega}/\left(\epsilon^{2}\tilde{D}_{b}\right)}\right)}{\mu \tilde{D}_{b} \sqrt{i\tilde{\omega}/\left(\epsilon^{2}\tilde{D}_{b}\right)}}$$
(46)

is the Warburg finite-length impedance. From Eq. (21) it follows that $\tilde{j}_{e,0}^1 = \tilde{\phi}_0^1/\tilde{Z}$. With this, Eq. (45) transforms to

$$\tilde{c}_*^1 = \frac{\tilde{Z}_W \tilde{\phi}_0^1}{\tilde{Z}} \tag{47}$$



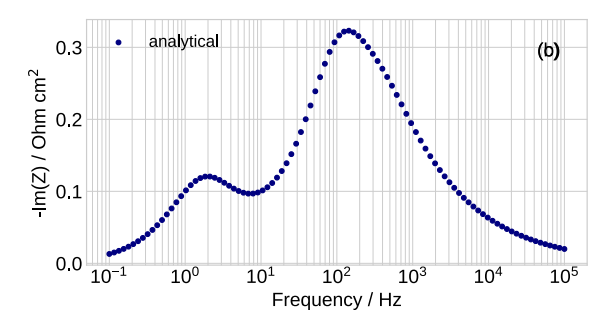


Fig. 6. (a) The analytical Nyquist spectrum of SOFC anode including hydrogen transport in the ASL, Eq. (50). The cell current density is 5 mA cm⁻²; the hydrogen pressure is 1 bar, the other parameters are collected in Table 1. (b) The Bode plot of imaginary part of impedance in (a).

Solving the system (27), (28), taking into account Eq. (47) and calculating the impedance, Eq. (21), we get an algebraic equation for \tilde{Z} . Solution to this equation yields the anode impedance \tilde{Z}_a :

$$\tilde{Z}_{a} = \frac{\tilde{R}_{c}^{0} \tilde{Z}_{W}}{\tilde{Q}_{c}^{0} + i\tilde{\omega}} + \frac{(1 + k_{\sigma}^{2}) \coth(p_{c}) + k_{\sigma} \left(p_{c} + 2/ \sinh(p_{c})\right)}{p_{c} k_{\sigma} (1 + k_{\sigma})}$$
(48)

where

$$p_{c} \equiv \frac{1}{\epsilon} \sqrt{\left(1 + 1/k_{\sigma}\right) \left(\tilde{Q}_{c}^{0} + i\tilde{\omega}\right)}. \tag{49}$$

Evidently, the first term in Eq. (48) is the ASL hydrogen transport impedance and the second term is the AAL impedance, Eq. (36), with p_c corrected for the hydrogen concentration factor. As expected, the ASL and AAL impedances are connected in series. Note that the transport impedance in Eq. (48) (the first term) differs from the Warburg finite-length impedance by the factor $1/(\tilde{Q}_c^0 + i\tilde{\omega})$, which is a parallel RC-circuit (reaction) impedance. This result means that the ASL impedance depends on the kinetics of the electrochemical reaction in the active layer, to which the ASL is attached (see [25] for discussion). Note that this feature cannot be described by ECM.

Finally, we note that for the anode-supported cells, it makes not much sense to take into account finite electron conductivity of the AAL, assuming that the ASL electron conductivity is infinite. In the limit of $k_\sigma \to \infty$, from Eq. (48) we get impedance of the anode with large electron conductivity:

$$\begin{split} \tilde{Z}_{a,k_{\sigma}\rightarrow\infty} &= \frac{\tilde{R}_{c}^{0}\tilde{Z}_{W}}{\tilde{Q}_{c}^{0}+\mathrm{i}\tilde{\omega}} \\ &+ \frac{1}{\sqrt{\left(\tilde{Q}_{c}^{0}+\mathrm{i}\tilde{\omega}\right)\left/\varepsilon^{2}}\tanh\left(\sqrt{\left(\tilde{Q}_{c}^{0}+\mathrm{i}\tilde{\omega}\right)\left/\varepsilon^{2}\right)}} \end{split} \tag{50}$$

The spectrum of Eq. (50) for the cell current density of 5 mA cm⁻² is depicted in Fig. 6. The low-frequency arc representing the ASL transport impedance is clearly seen (cf. Figs. 2 and 6).

3.3.1. Anode open-circuit impedance: fitting the experiment of Shi et al. [9]

Setting $\tilde{\eta}^0=0$ in Eqs. (29), from Eq. (50) we get the anode open-circuit impedance \tilde{Z}^{OCV}_o :

$$\begin{split} \tilde{Z}_{a}^{OCV} &= \left(\frac{\tilde{c}_{*}^{0} - 1}{\tilde{c}_{*}^{0} + \beta + \mathrm{i}\tilde{\omega}}\right) \frac{\tanh\left(\mu \tilde{I}_{b} \psi\right)}{\mu \tilde{D}_{b} \psi} \\ &+ \frac{1}{\sqrt{\left(\tilde{c}_{*}^{0} + \beta + \mathrm{i}\tilde{\omega}\right)/\varepsilon^{2}} \tanh\left(\sqrt{\left(\tilde{c}_{*}^{0} + \beta + \mathrm{i}\tilde{\omega}\right)/\varepsilon^{2}}\right)} \end{split} \tag{51}$$

where

$$\psi \equiv \sqrt{i\tilde{\omega}/\left(\epsilon^2\tilde{D}_b\right)} \tag{52}$$

Shi et al. [9] reported detailed experimental spectra of the button SOFC measured at open-circuit conditions. Assuming that the contribution of cathode side to the cell impedance is negligible, the spectrum from Shi et al. [9] has been fitted using the formula

$$Z_{cell} = \frac{l_a}{\sigma_i} \tilde{Z}_a^{OCV} + i\omega L_{cab} S_{cell} + R_{HFR}$$
 (53)

where L_{cab} is the cable inductance (H), and R_{HFR} is the cell high-frequency (ohmic) resistance. Seven parameters have been declared as fitting ones: the HOR Tafel slope $b_{hy}=RT/(\alpha_{hy}F)$, the AAL ionic conductivity σ_i , the effective volumetric double layer capacitance C_{dl} , the ASL effective hydrogen diffusivity D_b , the HOR volumetric exchange current density i_* , the high-frequency resistance R_{HFR} and the cable inductance L_{cab} . Based on preliminary fitting, the reference hydrogen concentration of $c_{hy,ref}=0.125c_{hy}$ has been used.

Experimental [9] and least-squares fitted model spectra are shown in Fig. 7. Though the quality of fitting is not perfect, the model describes the shape of the Nyquist spectrum reasonably well (Fig. 7a). In particular, the model captures two peaks of the imaginary part of impedance (Fig. 7b). The left (low-frequency) peak corresponds to the hydrogen transport through the ASL and the right peak is due to charge-transfer reaction. Note that the model returns well-resolved peaks, while in the experimental spectrum the peaks are smoothed (Fig. 7b). Fitting with Eq. (53) is extremely fast; it takes 2 s on a standard notebook to fit the spectrum in Fig. 7.

The upper part of Table 2 lists the cell operating parameters reported by Shi et al. [9]. The bottom part displays the anode parameters resulted from our fitting. Several comments to this Table need to be made

- The HOR Tafel slope b_{hy} is given per exponential basis; this value has to be multiplied by 2.303 to get the parameter per decade. The HOR transfer coefficient is calculated as $\alpha_{hy} = RT/(b_{hy}F)$; $\alpha = 1.02$ (Table 2) is somewhat lower than the values of 1.14 to 1.5 reported in the literature for Ni/YSZ anodes [11,26–28]. However, Shi et al. [9] used Ni/ScSZ anode active layer, which could explain lower α .
- The effective ASL hydrogen diffusivity $D_b \simeq 0.06~{\rm cm^2~s^{-1}}$ (Table 2) agrees well with the data measured by He et al. [29].
- The superficial exchange current density $i_{*,s} = i_* l_a$ is typically expressed as a function of the reacting gases composition [30]. In this work, the pressure-dependent factor is explicitly taken into account. For the temperature dependence of $i_{*,s}$ we use the following expression

$$i_{*,s} = \gamma_* \exp\left(\frac{-E_a}{RT}\right) \quad \text{A cm}^{-2}.$$
 (54)

with the pre-exponential factor γ_* and the activation energy E_a . For Ni/ScSZ electrodes, Fukumoto et al. [31] reported $\gamma_*=3.5\cdot 10^2$ A cm⁻² and $E_a=6.2\cdot 10^4$ J mol⁻¹ while Yonekura et al. [32] measured $\gamma_*=1.7\cdot 10^6$ A cm⁻² and $E_a=1.49\cdot 10^5$ J mol⁻¹. With the temperature T and electrode thickness l_a from Table 2, for the volumetric exchange current density $i_*=i_{*,s}/l_a$ Eq. (54) gives 224 A cm⁻³ with the data from Fukumoto et al. [31] and 63 A cm⁻³ with the data from Yonekura et al. [32]. The fitted parameter i_* (Table 2) is one order of magnitude smaller than the one calculated with Fukumoto et al. [31] parameters and it agrees

Upper part: The working cell parameters as reported by Shi et al. [9,39]. Bottom part: The anode parameters resulted from fitting of the spectrum in Fig. 7.

Cell temperature T , K	273 + 800
Total anode pressure p, kPa	101.325
Hydrogen partial pressure p_{hy} ,	0.958p
Reference H_2 pressure, $p_{hy,ref}$	$0.125p_{hy}$
Water vapor partial pressure p_w	0.042p
Reference water pressure $p_{w,ref}$	0.042p
ASL thickness l_b , μm	680 [39]
AAL thickness l_a , μm	15 [39]
Cell active area, S_{cell} , cm ²	1.54 [39]
Parameter $\beta = b_{hv}/b_w = \alpha_w/\alpha_{hv}$	1/3 [24]
, .,	
HOR Tafel slope b_{hy} , V/exp	0.0905
HOR Tafel slope b_{hy} , V/exp HOR transfer coefficient $\alpha_{hy} = RT/(b_{hy}F)$	0.0905 1.02
HOR transfer coefficient $\alpha_{hy} = RT/(b_{hy}F)$	1.02
HOR transfer coefficient $\alpha_{hy} = RT/(b_{hy}F)$ Double layer volumetric capacitance C_{dl} , F cm ⁻³	1.02 3.40
HOR transfer coefficient $\alpha_{hy} = RT/(b_{hy}F)$ Double layer volumetric capacitance C_{dl} , F cm ⁻³ Double layer superficial capacitance $C_{dl,s}$, F cm ⁻²	1.02 3.40 $5.1 \cdot 10^{-3}$
HOR transfer coefficient $\alpha_{hy} = RT/(b_{hy}F)$ Double layer volumetric capacitance C_{dl} , F cm ⁻³ Double layer superficial capacitance $C_{dl,s}$, F cm ⁻² Exchange current density i_* , A cm ⁻³	$ \begin{array}{c} 1.02 \\ 3.40 \\ 5.1 \cdot 10^{-3} \\ 28.2 \end{array} $
HOR transfer coefficient $\alpha_{hy} = RT/(b_{hy}F)$ Double layer volumetric capacitance C_{dl} , F cm ⁻³ Double layer superficial capacitance $C_{dl,s}$, F cm ⁻² Exchange current density i_* , A cm ⁻³ AAL ionic conductivity σ_i , S cm ⁻¹	1.02 3.40 $5.1 \cdot 10^{-3}$ 28.2 $1.65 \cdot 10^{-3}$
HOR transfer coefficient $\alpha_{hy} = RT/(b_{hy}F)$ Double layer volumetric capacitance C_{dl} , F cm ⁻³ Double layer superficial capacitance $C_{dl,s}$, F cm ⁻² Exchange current density i_* , A cm ⁻³ AAL ionic conductivity σ_i , S cm ⁻¹ ASL hydrogen diffusivity D_b , cm ² s ⁻¹	1.02 3.40 $5.1 \cdot 10^{-3}$ 28.2 $1.65 \cdot 10^{-3}$ 0.0592

well with the estimate using Yonekura et al. [32] data. Generally, i_* is difficult to estimate if two or more competing reactions occur in the electrode [33]. There is still an ongoing discussion of the HOR reaction mechanism and its rate-determining step(s) (see, e.g. Che et al. [34]).

The fitted volumetric double layer capacitance C_{dl} is related to the superficial electrode capacitance $C_{dl,s}$ as $C_{dl,s} = C_{dl}l_a$ (Table 2). Literature data on $C_{dl,s}$ in Ni/YSZ electrodes vary in the range of 10^{-4} to 10^{-3} F cm⁻². Takeda et al. [35] reported $C_{dl,s}$ = $(3.83 - 5.17) \cdot 10^{-4}$ F cm⁻², and Mohammadi et al. [36] measured $C_{dl,s} = 1.52 \cdot 10^{-4} \text{ F cm}^{-2}$. Takeda et al. [35] pointed out that the DL capacitance in an Ni/YSZ electrode arises from the oxygen ions at the metallic/ceramic interface, hence the crystal structure, doping and resulting oxygen ion concentration at the interface play a crucial role. YSZ has an order of magnitude smaller single crystal capacitance than ScSZ [37], hence an order of magnitude higher $C_{dl,s}$ in Table 2 is quite realistic. Further, $C_{dl,s}$ in Table 2 is not far from $C_{dl,s} = 2.7 \cdot 10^{-3}$ F cm⁻² measured by Shi et al. [9]. It is worth noting that Bertei et al. [38] reported the value of $C_{dl,s}$ for Ni/ScSZ electrodes two orders of magnitude smaller than our estimate (Table 2).

In summary, the fitted anode transport and kinetic parameters agree quite well with the literature data.

3.4. Concluding remarks

The models above are developed assuming that the active layer thickness is known. This assumption works well if the AAL ionic conductivity largely exceeds the ionic conductivity of support layer. In this case, all oxygen ions are converted in the AAL and the flux of ions through the AAL/ASL interface is negligible.

If, however, the AAL and ASL ionic conductivities are of the same order of magnitude, the effective AAL thickness is unknown in advance. Eqs. (50) and (51) still can be used for the experimental spectra fitting provided that l_a is declared as a fitting parameter. Due to finite ionic conductivity, the HOR rate rapidly decreases with the distance from the electrolyte. Our tests show that the length at which this rate is close to zero is recognized by the least-squares fitting procedure as an effective AAL thickness.

We found the cathode contribution to the impedance to be small in the measured frequency range. An attempt to add RC-circuit impedance in Eq. (53) as a model for the cathode reaction leads to formation of the third peak in the fitted model spectrum, which is absent

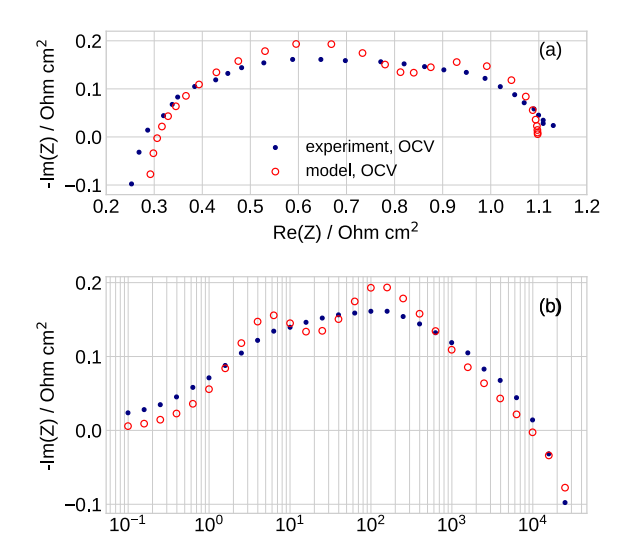


Fig. 7. (a) The experimental (solid points) and fitted model, Eq. (51), (open circles) Nyquist spectra of a button SOFC at open-circuit potential. The experimental points are digitized from Figure 6 of Shi et al. [9]. The cell operating parameters are listed in Table 2. (b) The Bode plot of imaginary part of impedance in (a).

10²

Frequency / Hz

10

10

10-

10⁰

in the experimental spectrum. Shi et al. [9] reported a negligible mass transport contribution from the cathode side. Montinaro et al. [40] emphasized the anode as a main contributor to the cell impedance in an anode supported SOFC. They mentioned that a noticeable contribution of the oxygen reduction reaction can be expected at frequencies below 1 Hz and potentials higher than 800 mV.

In numerous SOFC studies, equivalent circuit models (ECM) are still used for fitting experimental spectra (see [2] and the references cited therein). The main advantage of ECM is simplicity and fast fitting algorithms; however, models of that type are not reliable [3] and the ECM limits of validity are not clear. Eq. (36) provides a viable alternative to ECMs, as this equation is based on physical conservation laws, it has clear limits of validity, and it leads to fast fitting code. Furthermore, Eq. (36) can be used with standard fitting software supplied with EIS-meters by means of the user-defined functions mechanism. Being somewhat more complicated, the high-current model is also fast enough for using in fitting least-squares codes.

4. Conclusions

Analytical and numerical models for the button anode-supported SOFC impedance are developed. The models include the ion and electron charge conservation equations in the anode active layer (AAL) and the hydrogen mass transport equation in the anode support layer (ASL). The transport equations are linearized and Fourier-transformed to yield a system of linear ODEs for small AC perturbation amplitudes. In the limit of small cell current density, analytical solution of the linear system is obtained leading to a simple formula for the anode impedance. At high cell currents, the impedance can be calculated numerically using any standard boundary-value problem solver. Analytical impedance has been fitted to the spectrum of a button-cell measured at OCV by Shi et al. [9]. The resulting fitting parameters are in good agreement with literature data.

Nomenclature

Geometric Parameters:

x, X Spatial coordinate in x, X direction

l thickness, cm

Physical Constants and Properties i Imaginary unit

Electrochemical Parameters

 R_{HOR}, Q Reaction rate of the anode reaction,

 $A \text{ cm}^{-3}$

α Transfer coefficient

β Ratio of forward and backward

hydrogen reaction

b Tafel slope per V / exp

 i_* Exchange current density, A cm⁻³ E_a Activation energy for the anode

reaction, J mol-1

γ Reaction orderη Overpotential

 γ_{nre} Pre-exponential factor, A cm⁻²

Electrical Parameters

 C_{dl} Anode double layer capacitance per

F cm⁻³/ F cm⁻²

 L_{cab} Cable inductance, H

 k_{σ} Ratio of electron to ionic conductivity

 σ Conductivity

j current density

 Φ , ϕ Electric potential for ionic, electron

current

 ω Angular frequency

 R_{HFR} Cell high-frequency resistance, Ω cm²

Concentration and Pressure Parameters

 $\begin{array}{lll} c & \text{Available, reference concentration} \\ D & \text{Hydrogen diffusivity, cm}^2 \text{ s}^{-1} \\ p & \text{Total anode pressure, Pa} \\ p_{sub} & \text{Partial pressure, Pa} \end{array}$

Superscripts

0 Steady-state solution

Small-amplitude perturbation
 Marks dimensionless variables

Subscripts

hy Hydrogen, HOR
w Water, HER
ref Reference
a AAL
b ASL
i Ionic
e Electron
lim Limiting

Other Parameters

T Cell temperature, K

superficial

CRediT authorship contribution statement

S

Marisa Knappe: Writing – review & editing, Validation, Software, Investigation, Formal analysis, Data curation. Andrei Kulikovsky: Writing – review & editing, Writing – original draft, Visualization, Validation, Supervision, Software, Methodology, Investigation, Formal analysis, Conceptualization.

Declaration of competing interest

The authors declare that they have no known competing financial interests or personal relationships that could have appeared to influence the work reported in this paper.

References

- A. Lasia, Electrochemical Impedance Spectroscopy and Its Applications, Springer, New York, 2014.
- [2] Q.-A. Huang, R. Hui, B. Wang, J. Zhang, A review of AC impedance modeling and validation in SOFC diagnosis, Electrochim. Acta 52 (2007) 8144–8164, http://dx.doi.org/10.1016/j.electacta.2007.05.071.
- [3] D. Macdonald, Reflections on the history of electrochemical impedance spectroscopy, Electrochim. Acta 51 (2006) 1376–1388, http://dx.doi.org/10.1016/j.electacta.2005.02.107.
- [4] D. Harrington, P. van den Driessche, Mechanism and equivalent circuits in electrochemical impedance spectroscopy, Electrochim. Acta 56 (2011) 8005–8013, http://dx.doi.org/10.1016/j.electacta.2011.01.067.
- [5] J. Bisquert, Infuence of the boundaries in the impedance of porous film electrodes, Phys. Chem. Chem. Phys. 2 (2000) 4185–4192, http://dx.doi.org/ 10.1039/b001708f.
- [6] S. Devan, V. Subramanian, R. White, Analytical solution for the impedance of a porous electrode, J. Electrochem. Soc. 151 (2004) A905–A913, http://dx.doi. org/10.1149/1.1739218.
- [7] V. Sonn, A. Leonide, E. Ivers-Tiffée, Combined deconvolution and CNLS fitting approach applied on the impedance response of technical Ni/8YSZ cermet electrodes, J. Electrochem. Soc. 155 (2008) B675–B679, http://dx.doi.org/10. 1149/1.2908860.
- [8] J. Nielsen, J. Hjelm, Impedance of SOFC electrodes: A review and a comprehensive case study on the impedance of LSM:YSZ cathodes, Electrochim. Acta 115 (2014) 31–45, http://dx.doi.org/10.1016/j.electacta.2013.10.053.
- [9] Y. Shi, N. Cai, C. Li, C. Bao, E. Croiset, J. Qian, Q. Hu, S. Wang, Simulation of electrochemical impedance spectra of solid oxide fuel cells using transient physical models, J. Electrochem. Soc. 155 (3) (2008) B270, http://dx.doi.org/ 10.1149/1.2825146.
- [10] Y. Shi, H. Wang, N. Cai, Direct two-dimensional electrochemical impedance spectra simulation for solid oxide fuel cell, J. Power Sources 208 (2012) 24–34, http://dx.doi.org/10.1016/j.jpowsour.2012.02.012.
- [11] H. Zhu, R. Kee, Modeling elementary heterogeneous chemistry and electrochemistry in solid oxide fuel cells, J. Electrochem. Soc. 153 (2006) A1765–A1772, http://dx.doi.org/10.1149/1.2220065.
- [12] A. Kromp, H. Geisler, A. Weber, E. Ivers-Tiffée, Electrochemical impedance modeling of gas transport and reforming kinetics in reformate fueled solid oxide fuel cell anodes, Electrochim. Acta 106 (2013) 418–424, http://dx.doi.org/10. 1016/j.electacta.2013.05.136.
- [13] P. Hofmann, K. Panopoulos, Detailed dynamic solid oxide fuel cell modeling for electrochemical impedance spectra simulation, J. Power Sources 195 (2010) 5320–5339, http://dx.doi.org/10.1016/j.jpowsour.2010.02.046.
- [14] W. Bessler, Rapid impedance modeling via potential step and current relaxation simulations, J. Electrochem. Soc. 154 (2007) B1186–B1191, http://dx.doi.org/ 10.1149/1.2772092.
- [15] W. adn S. Gewies, Gas concentration impedance of solid oxide fuel cell anodes ii. Channel geometry, J. Electrochem. Soc. 154 (2007) B548–B559, http://dx. doi.org/10.1149/1.2720639.
- [16] A. Häffelin, J. Joos, M. Ender, A. Weber, E. Ivers-Tiffée, Time-dependent 3D impedance model of mixed-conducting solid oxide fuel cell cathodes, J. Electrochem. Soc. 160 (2013) F867–F876, http://dx.doi.org/10.1149/2. 093308ies
- [17] Y. Fu, Y. Jiang, S. Poizeau, A. Dutta, A. Mohanram, J. Pietras, M. Bazant, Multicomponent gas diffusion in porous electrodes, J. Electrochem. Soc. 162 (2015) F613–F621, http://dx.doi.org/10.1149/2.0911506jes.
- [18] A. Donazzi, S. Pascali, F. Garavaglia, M. Bracconi, A quasi 2D model for the interpretation of impedance and polarization of a planar solid oxide fuel cell with interconnects, Electrochim. Acta 365 (2021) 137346, http://dx.doi.org/10. 1016/j.electacta.2020.137346.
- [19] A. Kulikovsky, A model for impedance of a PEM fuel cell cathode with poor electron conductivity, J. Electroanal. Chem. 801 (2017) 122–128, http://dx.doi. org/10.1016/j.jelechem.2017.07.038.
- [20] L. de Haart, J. Mougin, O. Posdziech, J. Kiviaho, N. Menzler, Stack degradation in dependence of operation parameters; the real-sofc sensitivity analysis, Fuel Cells 9 (2009) 794–804, http://dx.doi.org/10.1002/fuce.200800146.
- [21] N. Menzler, D. Sebold, O. Guillon, Post-test characterization of a solid oxide fuel cell stack operated for more than 30,000 hours: The cell, J. Power Sources 374 (2018) 69–76, http://dx.doi.org/10.1016/j.jpowsour.2017.11.025.
- [22] B. Prakash, S. Kumar, S. Aruna, Properties and development of Ni/YSZ as an anode material in solid oxide fuel cell: A review, Renew. Sustain. Energy Rev. 36 (2014) 149–179, http://dx.doi.org/10.1016/j.rser.2014.04.043.

- [23] A. Kulikovsky, M. Eikerling, Analytical solutions for impedance of the cathode catalyst layer in PEM fuel cell: Layer parameters from impedance spectrum without fitting, J. Electroanal. Chem. 691 (2013) 13–17, http://dx.doi.org/10. 1016/i.ielechem.2012.12.002.
- [24] H. Zhu, R. Kee, Modeling electrochemical impedance spectra in SOFC button cells with internal methane reforming, J. Electrochem. Soc. 153 (2006) A1765–A1772, http://dx.doi.org/10.1149/1.2220065.
- [25] A. Kulikovsky, Why impedance of the gas diffusion layer in a PEM fuel cell differs from the Warburg finite-length impedance? Electrochem. Comm. 84 (2017) 28–31, http://dx.doi.org/10.1016/j.elecom.2017.09.014.
- [26] A. Leonide, Y. Apel, E. Ivers-Tiffee, Sofc modeling and parameter identification by means of impedance spectroscopy, ECS Trans. 19 (20) (2009) 81–109, http: //dx.doi.org/10.1149/1.3247567.
- [27] A. Utz, H. Störmer, A. Leonide, A. Weber, E. Ivers-Tiffée, Degradation and relaxation effects of Ni patterned anodes in $\rm H_2$ $\rm H_2O$ atmosphere, J. Electrochem. Soc. 157 (6) (2010) B920, http://dx.doi.org/10.1149/1.3383041.
- [28] J. Njodzefon, B. Sudireddy, J. Hjelm, C. Graves, Kinetic studies on Ni-YSZ composite electrodes, ECS Trans. 68 (1) (2015) 1169, http://dx.doi.org/10.1149/ 06801.1169ecst.
- [29] W. He, K. Yoon, R. Eriksen, S. Gopalan, S. Basu, U. Pal, Out-of-cell measurements of H₂-H₂O effective binary diffusivity in the porous anode of solid oxide fuel cells (SOFCs), J. Power Sources 195 (2010) 532–535, http://dx.doi.org/10.1016/ j.jpowsour.2009.07.051.
- [30] P. Costamagna, P. Costa, V. Antonucci, Micro-modelling of solid oxide fuel cell electrodes, Electrochim. Acta 43 (1998) 375–394, http://dx.doi.org/10.1016/ S0013-4686(97)00063-7.
- [31] T. Fukumoto, N. Endo, K. Natsukoshi, Y. Tachikawa, G. Harrington, S. Lyth, J. Matsuda, K. Sasaki, Exchange current density of reversible solid oxide cell electrodes, Int. J. Hydrog. Energy 47 (37) (2022) 16626–16639, http://dx.doi. org/10.1016/j.iihydene.2022.03.164.
- [32] T. Yonekura, Y. Tachikawa, T. Yoshizumi, Y. Shiratori, K. Ito, K. Sasaki, Exchange current density of solid oxide fuel cell electrodes, ECS Trans. 35 (1) (2011) 1007, http://dx.doi.org/10.1149/1.3570081.

- [33] S. Beale, M. Andersson, C. Boigues-Muñoz, H. Frandsen, Z. Lin, S. McPhail, M. Ni, B. Sundén, A. Weber, A. Weber, Continuum scale modelling and complementary experimentation of solid oxide cells, Prog. Energy Combust. Sci. 85 (2021) 100902, http://dx.doi.org/10.1016/j.pecs.2020.100902.
- [34] F. Che, S. Ha, J.-S. McEwen, Hydrogen oxidation and water dissociation over an oxygen-enriched ni/ysz electrode in the presence of an electric field: A first-principles-based microkinetic model, Ind. Eng. Chem. Res. 56 (5) (2017) 1201–1213, http://dx.doi.org/10.1021/acs.iecr.6b04028.
- [35] M. Takeda, K. Yashiro, R. Budiman, S. Hashimoto, T. Kawada, Study of Ni-YSZ electrode capacitance and its correlation with the microstructure, J. Electrochem. Soc. 170 (3) (2023) 034505, http://dx.doi.org/10.1149/1945-7111/acc1a4.
- [36] R. Mohammadi, M. Søgaard, T. Ramos, M. Ghassemi, M. Mogensen, Electro-chemical impedance modeling of a solid oxide fuel cell anode, Fuel Cells 14 (4) (2014) 645–659, http://dx.doi.org/10.1002/fuce.201300292.
- [37] A. Kezionis, S. Kazlauskas, D. Petrulionis, A. Orliukas, Broadband method for the determination of small sample's electrical and dielectric properties at high temperatures, IEEE Trans. Microw. Theory Tech. 62 (10) (2014) 2456–2461, http://dx.doi.org/10.1109/TMTT.2014.2350963.
- [38] A. Bertei, E. Ruiz-Trejo, F. Tariq, V. Yufit, A. Atkinson, N. Brandon, Validation of a physically-based solid oxide fuel cell anode model combining 3d tomography and impedance spectroscopy, Int. J. Hydrogen Energy 41 (47) (2016) 22381–22393, http://dx.doi.org/10.1016/j.ijhydene.2016.09.100.
- [39] Y. Shi, N. Cai, C. Li, C. Bao, E. Croiset, J. Qian, Q. Hu, S. Wang, A general approach for electrochemical impedance spectroscopy simulation using transient mechanistic SOFC model, ECS Trans. 7 (2007) 1889–1899, http://dx.doi.org/10. 1149/1.2729301.
- [40] D. Montinaro, A. Contino, A. Dellai, M. Rolland, Determination of the impedance contributions in anode supported solid oxide fuel cells with (La, Sr)(Co, Fe)O₃-δ cathode, Int. J. Hydrogen Energy 39 (2014) 21638–21646, http://dx.doi.org/10. 1016/j.ijhydene.2014.09.081.